Additive Manufacturing 32 (2020) 101087

Contents lists available at ScienceDirect

Additive Manufacturing

journal homepage: www.elsevier.com/locate/addma

Full Length Article

Anisotropic tensile behavior of Ti-47Al-2Cr-2Nb alloy fabricated by direct laser deposition

Xinyu Zhang[a], Chuanwei Li[b,**], Mengyao Zheng[a], Zhenhua Ye[a], Xudong Yang[a], Jianfeng Gu[a,c,*]

[a] Institute of Materials Modification and Modelling, School of Materials Science and Engineering, Shanghai Jiao Tong University, Shanghai 200240, China
[b] Materials Genome Initiative Center, Shanghai Jiao Tong University, Shanghai 200240, China
[c] Shanghai Key Laboratory of Materials Laser Processing and Modification, Shanghai Jiao Tong University, Shanghai 200240, China

ARTICLE INFO

Keywords:
TiAl alloy
Direct laser deposition
Anisotropic tensile behavior
Deformation mechanism
Fracture mechanism

ABSTRACT

Additive manufacturing is emerging as an increasingly promising technology for TiAl alloys, which are attracting significant attention for their special microstructure and mechanical properties. In the present study, direct laser deposition was applied to fabricate single-track Ti-47Al-2Cr-2Nb alloy walls with a back-and-forth scanning strategy. The resulting alternative-band microstructure, comprising complicated microstructure bands and coarse lamellar colony bands, was characterized, and electronic back-scatter diffraction analysis showed that the lamellae in coarse colonies present a consistent orientation, nearly parallel to the substrate. The tensile properties of the as-deposited specimens varied greatly with the angle (θ) between the loading direction and the substrate. The specimens exhibited the best comprehensive tensile properties of the maximum ultimate strength and elongation (706 MPa and 0.51 %) with the loading direction parallel to the substrate (θ= 0°). The ultimate strength and elongation dropped to minimum values of 273 MPa and 0.16 %, respectively, when the loading direction was perpendicular to the substrate (θ= 90°). At the middle state of loading direction, θ= 45°, the ultimate strength decreased to 358 MPa, and the elongation remained as high as 0.49 %. Transmission electron microscopy observations revealed that dislocations and deformation twinning were both activated under different loading modes, and their morphologies were dramatically different. The formation mechanism of the alternative-band microstructure was proposed from the aspects of rapid solidification and the cyclic heat-treatment effect, and its possible fracture mechanism and crack propagation mode were discussed.

1. Introduction

TiAl alloys are among the most popular high-temperature structural materials motivated by the development of lightweight and high-efficiency aeroengines, which are attracting massive interest because of their low density, high specific strength, and excellent creep resistance at elevated temperatures [1]. However, considerable challenges in fabricating and shaping such extremely brittle intermetallic alloys make the end products exceedingly expensive compared with Ti alloys or Ni superalloys [2]. Thus, it is of great significance to develop methods capable of producing net or near-net shape parts with acceptable costs.

Additive manufacturing (AM), which mainly includes three different methods: selective laser melting (SLM), electron beam melting (EBM) and direct laser deposition (DLD), is a novel manufacturing method based on the layer-by-layer fusion of powder feedstock [3]. Its greatest advantage is the high fabrication freedom that allows for the production of fully dense 3-dimensional parts with various geometric features without additional equipment [4]. The microstructure and corresponding mechanical properties of the additively manufactured components sometimes exhibit complicated characteristics that are significantly different from those of components obtained by traditional casting or forging. Because each built location is subjected to a unique and cyclic thermal history, including first rapid solidification, multiple fast heating, and cooling heat treatments, a heterogeneous microstructure deviating from the equilibrium state results [5]. Moreover, the nature of the partial remelting of the previous layers and its large thermal gradient in the melt pool result in an epitaxial growth of grains, which potentially creates an intrinsic texture that gives rise to anisotropic mechanical properties [6]. The properties of additively manufactured parts potentially determine their applications and ultimate

* Corresponding author at: Institute of Materials Modification and Modelling, School of Materials Science and Engineering, Shanghai Jiao Tong University, Shanghai 200240, China.
** Corresponding author.
E-mail addresses: li-chuanwei@sjtu.edu.cn (C. Li), gujf@sjtu.edu.cn (J. Gu).

https://doi.org/10.1016/j.addma.2020.101087
Received 20 October 2019; Received in revised form 21 January 2020; Accepted 22 January 2020
Available online 25 January 2020

failure modes. Therefore, exploring the detailed anisotropic behavior of additively manufactured alloys and relating it to the specific microstructure are of great significance. Previous investigations mainly concentrated on austenitic stainless steel [7–9] and Ti alloys [10,11], revealing similar anisotropic behaviors in which the ultimate strength of uniaxial tensile along the vertical direction appears to be slightly lower than the horizontal samples. However, the corresponding elongation was higher when the samples were loaded along the vertical direction compared with the horizontal direction. The anisotropic behavior was attributed to the columnar morphology of the austenite (in stainless steel) or β grains (in Ti alloys), and the boundaries of these columnar grains served as pathways along which cracks preferentially accumulated and propagated, leading to the final fractures [11].

Additively manufactured TiAl alloys have also received considerable attention, and studies have mainly focused on processing optimization and microstructure characterization. Schwerdtfeger et al. [12] reported a broad parameter window for processing Ti-48Al-2Cr-2Nb (at.%) alloy, establishing the relationship between the chemical composition variations, process parameters and scanning strategy, and achieving a wide range of microstructures varying from lamellar to massively transformed γ. Li et al. [13–16] comprehensively investigated the effect of energy density input, substrate preheating, heat treatment, and TiB_2 addition on the texture evolution, phase transformation mechanisms, and nanohardness of additively manufactured Ti-45Al-2Cr-5Nb alloy. Thomas et al. [17] optimized the process parameters and successfully prevented cracking, which is otherwise observed in the brittle material, induced by the large stress caused by fast cooling and thermal cycling history. They obtained superior tensile properties compared with the cast samples. Thus far, there have been few published works reporting on the anisotropic mechanical behavior of additively manufactured TiAl alloys and the effect of microstructure.

In the present study, the microstructure and tensile mechanical properties of Ti-47Al-2Cr-2Nb alloy, fabricated using DLD method, are carefully investigated, and the emphasis is placed on the anisotropic behavior of the tensile properties when the as-deposited samples are loaded along different directions (the angle between tensile direction and the substrate are set as 0°, 45°, and 90°, respectively). An alternative-band microstructure composed of alternating complicated microstructure bands and coarse lamellar colony bands, and the anisotropic behavior different from other reports of titanium alloys and stainless steel are observed. The possible deformation and fracture mechanisms underlying are also discussed.

2. Experimental

2.1. Materials and methods

Ti-47Al-2Cr-2Nb (at.%) pre-alloyed powder, prepared by electrode induction melting gas atomization, was utilized as the deposition raw material, and its chemical composition was measured, as presented in Table 1. It can be seen that the actual chemical composition is very close to the nominal composition. A DLD system equipped with an Yt fiber laser was used to fabricate single-track walls (40 × 50 × 2 mm), as shown in Fig. 1. The single-track walls were deposited on a 100 × 100 × 10-mm Ti-48Al plate with a back-and-forth scanning strategy in a high-purity Ar chamber. The process parameters were set as follows: laser power 400 W; scanning speed 4 mm/s; feeding rate 3 g/min; and layer thickness 0.3 mm.

Table 1
Chemical composition of the as-received powder and as-deposited specimen in at.% and wt.%, respectively.

	Elemental chemical composition			
	Ti	Al	Cr	Nb
(at.%)				
Powder as received	Bal.	47.7	1.86	2.05
Specimen as deposited	Bal.	45.9	1.94	1.95
(wt.%)				
Powder as received	Bal.	33.1	2.5	4.9
Powder as deposited	Bal.	31.5	2.6	4.6

2.2. Microstructure characterization

The microstructure morphologies were examined using an optical microscope (OM) and scanning electron microscope (SEM) following a standard specimen preparation procedure. Electron backscatter diffraction (EBSD) was performed using a TESCAN Lyra3 Gum field emission microscope operated at 20 kV. Local scan areas of 400 × 400 μm and 100 × 100 μm were used for EBSD analysis with a step size of 0.4 and 0.1 μm, respectively. EBSD data was analyzed using the Channel 5 software provided by Oxford. The chemical composition was measured using an energy dispersion spectrum detector included with the SEM. Phase constitution was identified through X-ray diffraction (XRD) on a poly-functional X-Ray diffractometer with 2θ varying from 20° to 120°. An FEI Talos F200X transmission electron microscope (TEM) was used at 200 kV to investigate more detailed microstructures. TEM specimens of as-deposited samples were prepared via precision cutting and subsequently ground to a thickness of 100 μm, followed by twin-jet at ~30 V with a reagent (59 vol.% methanol, 35 vol.% butanol, and 6 vol.% perchloric acid). Samples examined for their deformation behaviors were obtained through focused ion beam milling near the fracture.

2.3. Mechanical tests

Three kinds of dog-bone specimens having a gauge section of 6 mm (length) × 2 mm (width) × 1.5 mm (thickness) were machined from the deposited walls for tensile tests, as shown in Fig. 1b. The geometry and dimensions of these specimens were designed as non-proportional specimens according to International Standard ISO-6892-1. The angles between the tensile direction and the substrate were 0°, 45°, and 90°, respectively. All specimens were prepared using the standard grinding and polishing procedure to eliminate the effects of surface roughness. Uniaxial tensile experiments were conducted on a 5-kN screw machine at a displacement rate of 0.1 mm/min under an in situ optical microscope. The speckle pattern on the gauge section prepared prior to tensile testing was traced from the optical images, used as the extensometer. The strain-field contours were calculated using a digital image correlation method. Vickers hardness along the building direction on the polished specimens was measured using a Fischerscope HM200 microhardness tester.

3. Results

3.1. Alternative-band microstructure of Ti-47Al-2Cr-2Nb alloy fabricated by DLD

Fig. 2 presents the XRD patterns obtained from the vertical cross section of the as-deposited Ti-47Al-2Cr-2Nb alloy, used to identify the phase constitution. Most of the diffraction peaks corresponded to the α_2 and γ phases, and no β phase was detected. Moreover, many forked peaks were observed in the diffraction pattern, resulting from the tetragonal crystal structure of the γ phase. A semi-quantitative calculation from the diffraction pattern indicated that the molar fractions of α_2 and γ were respectively 7.25 and 92.75 %, which deviates from the equilibrium state according to the phase diagram measured by Schuster [21]. The chemical composition of the as-deposited specimens is presented in Table 1, where the associated Al content is approximately 2 at.% lower when compared with the precursor powder. As was reported in previous studies [18,19], Al loss is a common phenomenon during

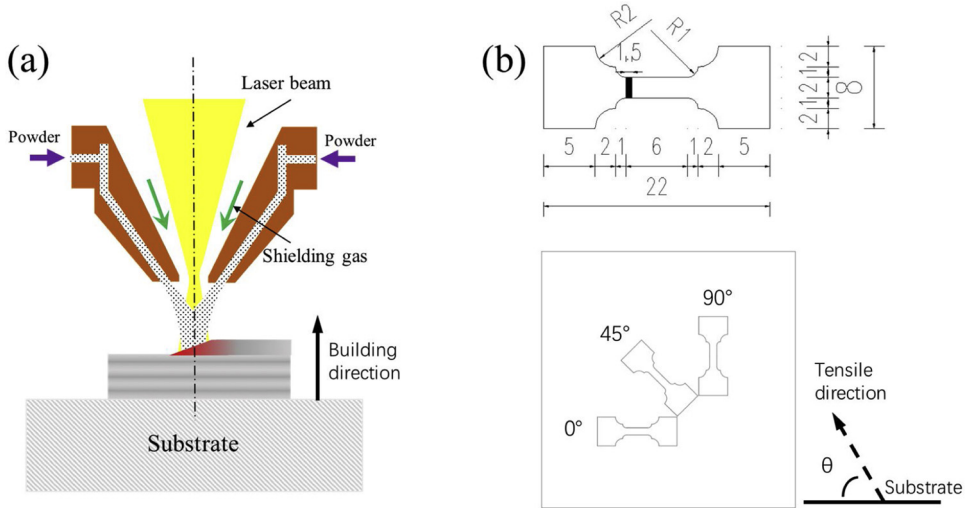

Fig. 1. (a) Schematic of the direct laser deposition process; (b) Tensile specimen geometry and their orientations (the angles θ between tensile direction and the substrate are 0°, 45°, and 90°, respectively); all dimensions are in mm.

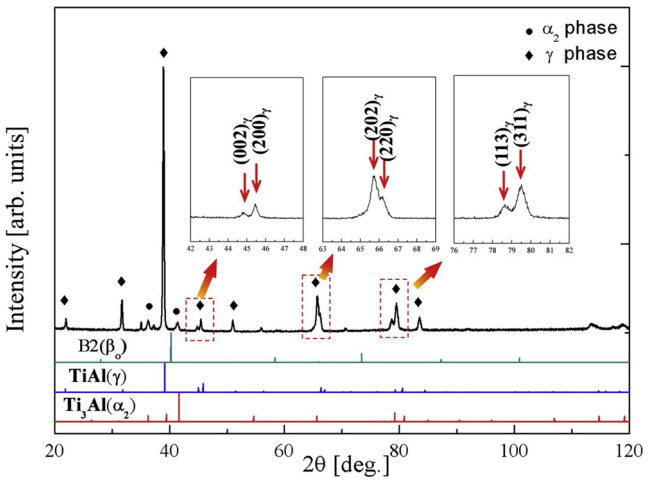

Fig. 2. XRD patterns of the vertical cross section of the as-deposited Ti-47Al-2Cr-2Nb specimen, compared with the standard diffraction patterns of Ti_3Al (α_2), TiAl(γ) and B2(β_o). The images in the inset are the magnified patterns of the peaks denoted by dashed rectangles.

additive manufacturing, because the high energy density usually contributes to significant overheating, leading to Al vaporization.

Fig. 3 shows the general microstructure of the as-deposited specimen. Cracks caused by thermal stress were rarely observed, but a few spherical pores 1–2 μm in size did appear. This was the result of gas trapping in the melt pool. The total porosity of this specimen was measured to be approximately 0.2 %, and the associated density was 3.825 g/cm^3, demonstrating that the process parameters used in the present study enabled the production of a nearly fully dense Ti-47Al-2Cr-2Nb alloy specimen. Moreover, it is worth noting that two different bands having dark and bright contrast were alternatively arranged along the building direction, clearly distinguished in the OM image (Fig. 3a). From the SEM-BSE image (Fig. 3b), it was observed that the dominating microstructure feature is a dendritic morphology, which is considered to originate from the solidification behavior that causes chemical composition segregation [20]. The SEM-BSE mode reflects the contrast based on chemical composition and the places where heavy elements aggregate, which always exhibit a bright contrast. Thus, it was deduced that Ti prefers to gather at the bright dendritic zones, whereas Al tends to be enriched at the dark interdendritic zones. Additionally, alternative bands can be recognized because of the different compositions of the interdendritic zone of each band, as reflected in Fig. 3b. Figs. 3c and 3d are respectively the magnified SEM-BSE images corresponding to the locations in Fig. 3b. It can be seen in Fig. 3c that the interdendritic zones consist of fine equiaxed γ phase, feathery microstructures, and Widmanstatten laths with various orientations. Furthermore, the dendrite zones are always coarse lamellar colonies, which, as a result, constitute a so-called complicated microstructure band. However, the other band completely consists of coarse lamellar colonies, and nearly all these laths are directional and parallel to the substrate with less than 20° deviations (Fig. 3d). Thus, it was concluded that the alternative-band, comprising a complicated microstructure band and coarse lamellar colony band, was the main microstructure feature of the as-deposited specimen. The average thicknesses of the complicated microstructure band and the directional coarse lamellar band were measured to be 131 ± 16 μm and 187 ± 21 μm, respectively. The sum corresponds approximately to the layer thickness of each deposition track during DLD, suggesting that the formation of this alternative-band microstructure was closely related to the layer-by-layer building mode.

EBSD images were used to describe microstructure morphology more visually and to allow for statistical analysis of grain orientations, as shown in Fig. 4. It can be seen that the profile of the prior grains exhibits coarse columnar morphology that appears to result from epitaxial growth beyond a single layer thickness. Within these prior grains, the α_2 and γ phases always present a lamellar structure nearly parallel to the substrate (Fig. 4c). In Fig. 4d, the pole figure of the α_2 phase suggests that all the measured α_2 phase possesses a common orientation of the {0001} plane. In the {11$\bar{2}$0} pole figure, two series of three {11$\bar{2}$0} planes of the α_2 phase, distinguished by different intensities, were observed deviating from each other by a relatively low angle. Furthermore, the statistical analysis of the boundaries of the α_2 phase indicates that the misorientation angles of nearly all the α_2 grain boundaries are under 10°, implying all of the α_2 grains possess a constant crystal orientation. In the pole figure of the γ phase (Fig. 4e), the {111} and {110} planes, denoted by circles and squares, respectively, correspond to the {0001} and {11$\bar{2}$0} planes of the α_2 phase, indicating a Blackburn orientation relationship: $\{111\}_\gamma \,||\, \{0001\}_{\alpha 2}$ and $<1\bar{1}0>_\gamma \,||\, <11\bar{2}0>_{\alpha 2}$ [22]. It can also be observed that there are a large number of γ twins existing in the prior columnar grains (Fig. 4a), and the γ twins share a common (111) plane with the matrix (Fig. 4e). From the misorientation distribution histogram, it is known that many γ boundaries form the special angles of 60°, 70°, and 90°. Beyond that, the alternative-band microstructure morphology was also distinguished in these EBSD images, coinciding with the above observations. Fig. 5 presents the

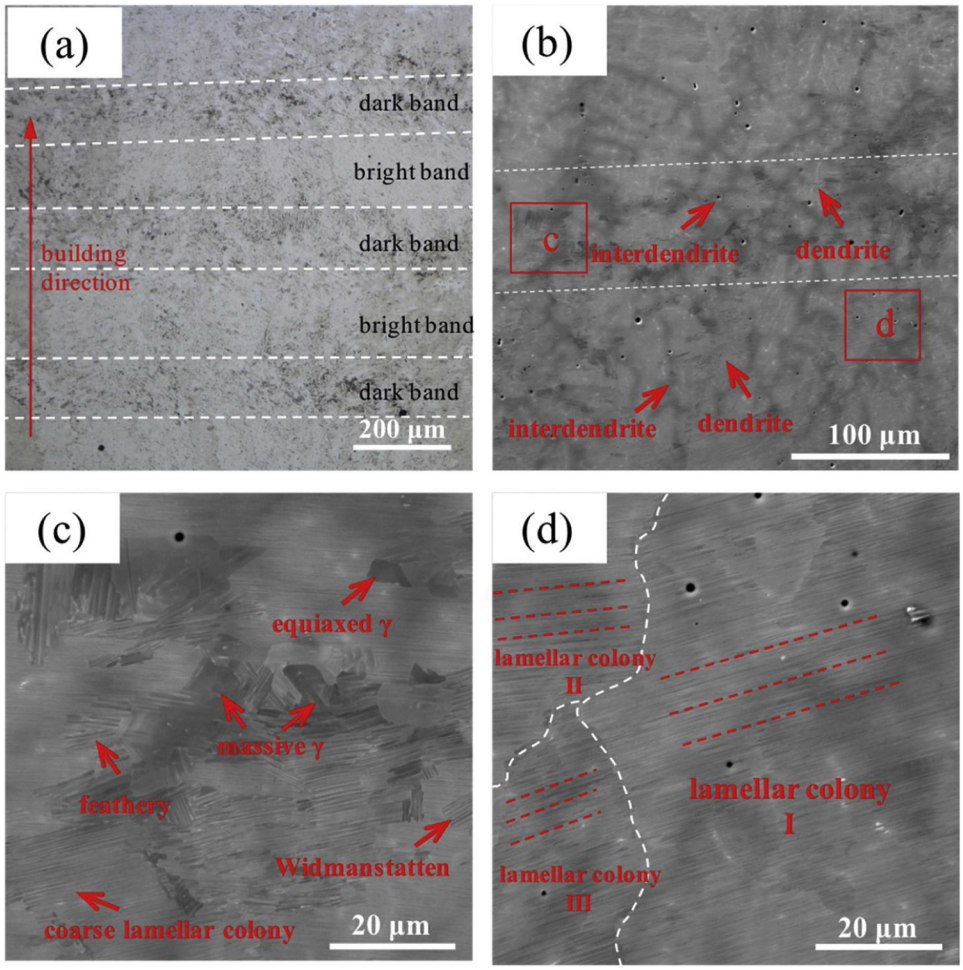

Fig. 3. Alternative-band microstructure of an as-deposited specimen comprising fine complicated structure bands and directional lamellar bands. (a) OM image; (b) SEM-BSE image; (c) and (d) Magnified SEM-BSE images corresponding to the locations noted in (b), showing the microstructure morphology of the fine complicated structure band and the directional lamellar band.

inverse pole figures of the complicated microstructure band and coarse lamellar colony band and their associated pole figures. In the complicated microstructure band (Fig. 5a), the feathery structure and equiaxed γ phase are inserted at the boundaries of coarse columnar colonies. Regarding the coarse lamellar colony boundary, these boundaries simply connect two columnar lamellar colonies (Fig. 5c), and the misorientation between them is very small, thus forming low-angle boundaries as denoted by the black lines. The pole figures of the γ phase (Figs. 5b and d) show that the crystal orientation of the complicated microstructure band is promiscuous and irregular, whereas, in the coarse lamellar colony band, it seems constant. The accumulated seven points in the {111} pole figure are related to a pair of twin relationship γ phases inherited from one α/α_2 grain. Additionally, it was noticed that both the coarse lamellar structures in these two bands present a close crystal orientation, as judged by the same orientation colors made up of red and violet.

3.2. Microhardness distribution along building direction

The microhardness distribution over a range of 1000 μm along the building direction was measured, as shown in Fig. 6. The associated hardness distribution presents a periodic rise and fall around 400 HV. The maximum and minimum hardness values are respectively 438 and 356 HV. Moreover, the period of the hardness fluctuation is approximately 300 μm, which is in accordance with the period of the arrangement of alternative bands. The indentation places under OM reveals that the high-hardness indentations are located at coarse lamellar colony bands, whereas the low-hardness indentations are always distributed in the complicated microstructure bands.

3.3. Anisotropic tensile behavior of the as-deposited Ti-47Al-2Cr-2Nb alloy

In situ tensile tests were conducted to clarify the anisotropic tensile behavior of the alternative-band microstructure by loading along three different directions (θ= 0°, 45°, and 90°). The results are shown in Fig. 7a, and all the stress–strain curves show no obvious yield phenomenon, which is in accordance with stress–strain curves measured from parts fabricated by casting [23,24]. Additionally, it was observed that the ultimate strength and elongation were closely dependent on the loading direction. When the loading direction was parallel to the substrate (θ = 0°), the specimen exhibited the best comprehensive tensile behavior with the maximum ultimate strength and elongation (706 MPa and 0.51 %), which is a remarkable combination, even when compared with conventionally fabricated parts [23–29] (Fig. 7b). When the loading direction was inclined (θ = 45°), the tensile strength largely decreased to 358 MPa, but the elongation remained nearly unchanged. In this case, the strength was slightly lower than that of conventionally fabricated parts. Once the loading direction was turned perpendicular to the substrate (θ = 90°), both the ultimate strength and elongation dropped to their minimum values (273 MPa and 0.16 %), which is located at the left bottom corner of the strength–elongation diagram, indicating miserable tensile properties.

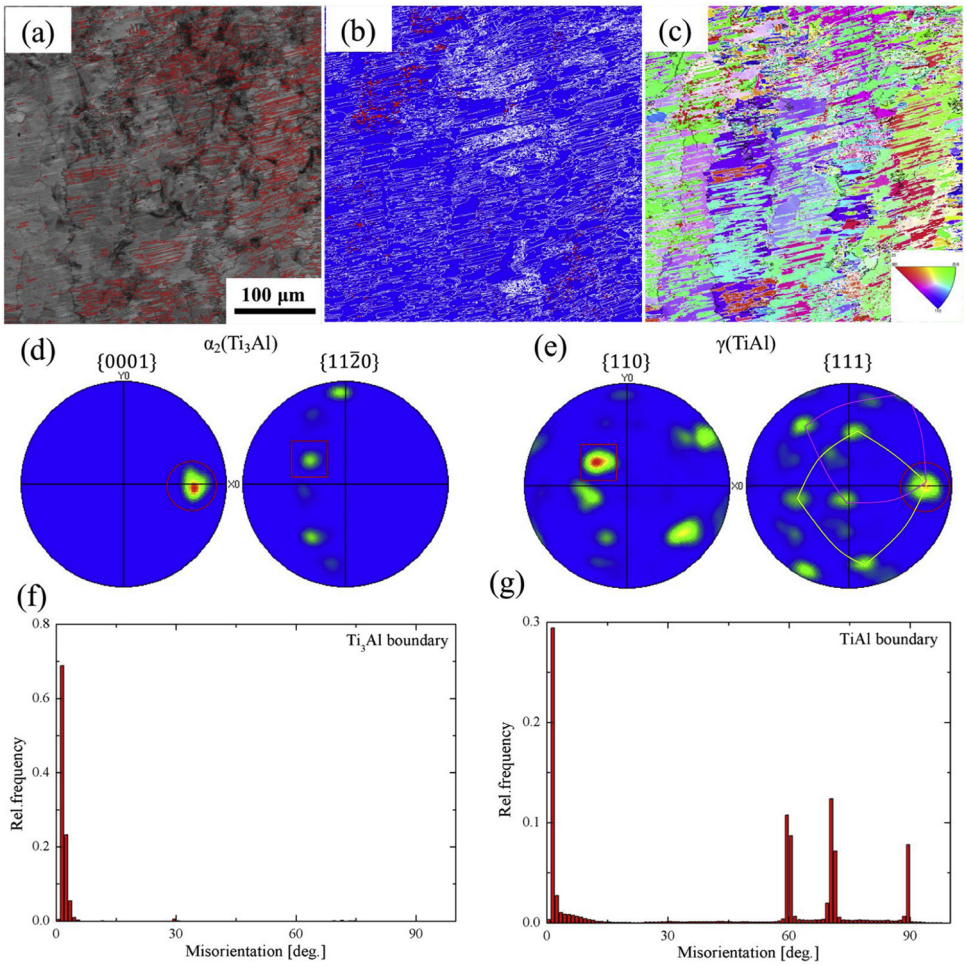

Fig. 4. EBSD images obtained from the as-deposited specimen with a region size of 400 × 400 μm. The red, black, and white lines represent Σ3 twin boundaries, 2–10° low-angle boundaries, and large-angle boundaries larger than 10°, respectively. (a) Band contrast; (b) Phase component where red represents the α_2 phase and blue represents the γ phase; (c) Inverse pole figure; (d) and (e) Pole figures of α_2 and γ phases; (f) and (g) Histograms representing the boundary misorientation distribution of α_2 and γ phases. (For interpretation of the references to colour in this figure legend, the reader is referred to the web version of this article).

The strain distribution maps at different engineering-strain levels are shown in Fig. 8a, and the line scanning maps indicating strain variation in the middle of the specimens are shown in Fig. 8b. It was obtained that the macro-deformation mode varied with loading orientations. For the specimen loaded at θ = 0°, which exhibited excellent tensile properties, no obvious macro-deformation bands were observed, and the deformation areas appeared non-directional and irregular. Meanwhile, the strain fluctuation along the gauge length is relatively gentle, and the maximum strain value is approximately 0.65. Regarding the specimen loaded at θ = 45°, it was observed that two wide macro-deformation bands, forming a 45° angle with the loading direction, were generated. The corresponding line-scanning map indicates that all the localized strain values exhibited a tendency to grow with increasing engineering strain. There were two obvious strain peaks extending to 0.76 and 0.9 % at the engineering strain of 0.5 %, which is larger than the average strain value. Moreover, the strain fluctuation appears more obvious than the specimen loaded at θ = 0°. When the loading direction is θ = 90°, multiple narrow deformation bands, denoted by blue color, appeared perpendicular to the loading direction. Moreover, with an increase in engineering strain, the strain fluctuation along the gauge length increased a lot. At an engineering strain of 0.16 %, the maximum strain value was 0.38 %, whereas the minimum strain value was only 0.03 %.

To investigate the deformation mechanism of the as-deposited specimens with different loading directions, TEM images of the coarse lamellar colonies around fracture surfaces were obtained. Fig. 9a shows the TEM morphology of the lamellar structure in an as-deposited specimen without loading applied. It can be seen that the lath width mainly ranged from 20 to 180 nm, and nearly no deformation twins or dislocations were observed. The inserted selected area electron diffraction (SAED) pattern reveals the Blackburn orientation relationship between the α_2 and γ laths, which agrees with the results obtained from EBSD. Moreover, the twinning relationship along the (111) plane between γ laths is also described by the yellow and green outlines in the SAED pattern. However, in the deformed specimens, deformation twins and dislocations appeared in the γ laths, and different loading directions induced various deformation modes. When the loading direction was parallel to the substrate (θ = 0°), the deformation twins presented a transverse morphology, and they were completely confined within single γ laths (Fig. 9b). When the loading direction was perpendicular to the substrate (θ = 0°), most of the deformation twins interacted greatly with the lamellar interfaces and traversed across several laths (Fig. 9d). However, when the loading direction was inclined (θ = 45°), the deformation twins and slip lines were parallel to the lamellar interfaces, and transverse deformation twins were rarely observed (Fig. 9c).

The cross-sections of fractures under different loading directions indicate the fracture mode and related crack propagation pathway, as shown in Figs. 10a–c. These images reveal that the fracture surface of the θ = 0° sample exhibited an irregular morphology, and the principal

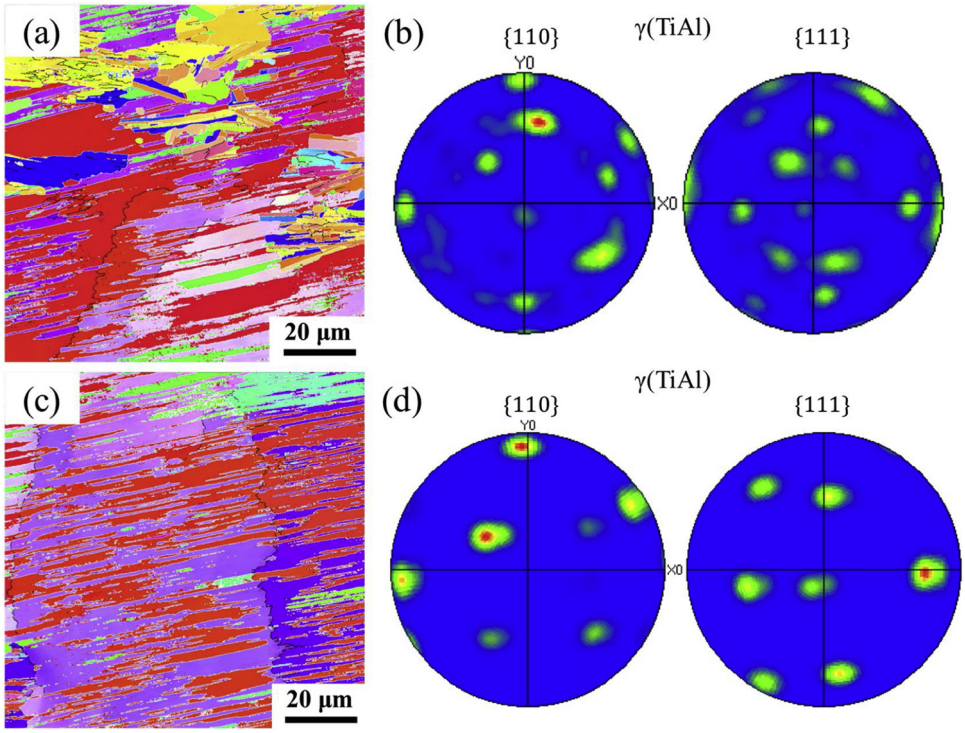

Fig. 5. EBSD images locally obtained from the as-deposited specimen with a region size of 100 × 100 μm. (a) and (b) Inverse pole figure of the complicated structure band and its associated pole figure of the γ phase, presenting a promiscuous crystal orientation; (c) and (d), Inverse pole figure of the coarse lamellar colony band and its associated pole figure of the γ phase.

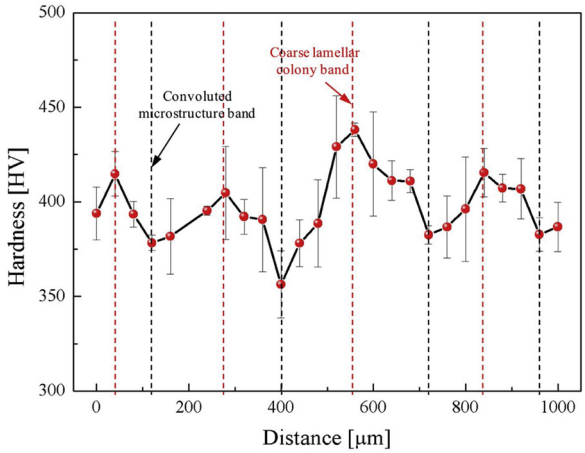

Fig. 6. Microhardness distribution along the building direction in the as-deposited Ti-47Al-2Cr-2Nb alloy specimens.

crack propagated vertically to the lamellar interfaces. However, for the sample of θ = 90°, the fracture surface was perpendicular to the loading direction (Fig. 10c) while that of the θ = 45° sample formed an approximately 45° angle with the loading direction (Fig. 10b), which corresponds to the macro-deformation bands in the strain distribution maps (Fig. 8c). Meanwhile, their principal cracks always propagated along the lamellar interfaces, contributing to a straight and flat fracture surface. Combined with the fracture surface morphologies of the different tensile specimens (Figs. 10d–i), it was deduced that intergranular fracture was the main feature of the θ = 45° and θ = 90° specimens, accompanied by some tearing of ligaments. However, the specimen loaded at θ = 0° usually presented translamellar fractures with sheet-like fracture morphologies (Figs. 10d and g). In the amplified fracture images (Fig. 10i), we can distinguish large numbers of nanolaths inserted in the γ plates of the specimen loaded at θ = 90°, which are considered as the result of transverse γ deformation twins, as marked by red arrows. However, in Fig. 10h, for the θ = 45° specimen, nanolaths were rarely discovered in the plates, in accordance with the TEM observation of no transverse deformation twins (Fig. 9).

4. Discussion

4.1. Microstructure formation mechanism

Based on the OM, SEM, and EBSD images, we can draw the conclusion that there are two major characteristics describing the microstructure morphology of the as-deposited Ti-47Al-2Cr-2Nb alloy. One is the alternative-band morphology comprising complicated microstructure bands and coarse lamellar colony bands, whereas the other is the overwhelming coarse lamellar colonies which always exhibit a columnar morphology growing along the building direction. The α_2/γ laths fill in these coarse colonies and present coincident and directional orientations, which are perpendicular to the columnar direction and nearly parallel to the laser scanning direction. Both features are associated with the unique thermal history.

First, we should discuss the formation mechanism of directional columnar lamellar colonies, which are largely related to solidification and solid-phase transformation. As is known, the solidification microstructure is strongly related to the solidification conditions [30–32]. Temperature gradient (G) and growth rate (V) play important roles in determining the solidification microstructural morphology, including columnar and equiaxed grains, which have been completely explored for Ni-based alloys [32]. To explore the microstructure formation mechanism, the columnar-to-equiaxed transition phenomenon must be considered.

According to Hunt's model [30], fully equiaxed growth occurs when

$$G<0.617N_0^{1/3}\left\{1-\frac{(\Delta T_N)^3}{(\Delta T_c)^3}\right\}\Delta T_c \quad (1)$$

and fully columnar growth occurs when

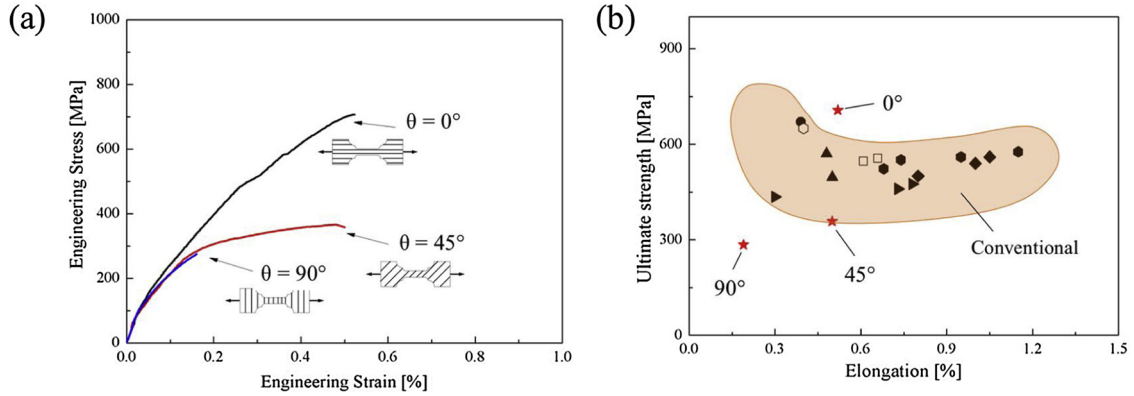

Fig. 7. (a) Tensile stress–strain curves of as-deposited specimens with different loading directions (θ = 0°, θ = 45°, and θ = 90°). The parallel lines highlight the orientation of alternative bands in the tensile specimens; (b) Tensile property of Ti-47Al-2Cr-2Nb alloy fabricated by DLD and the conventional method.

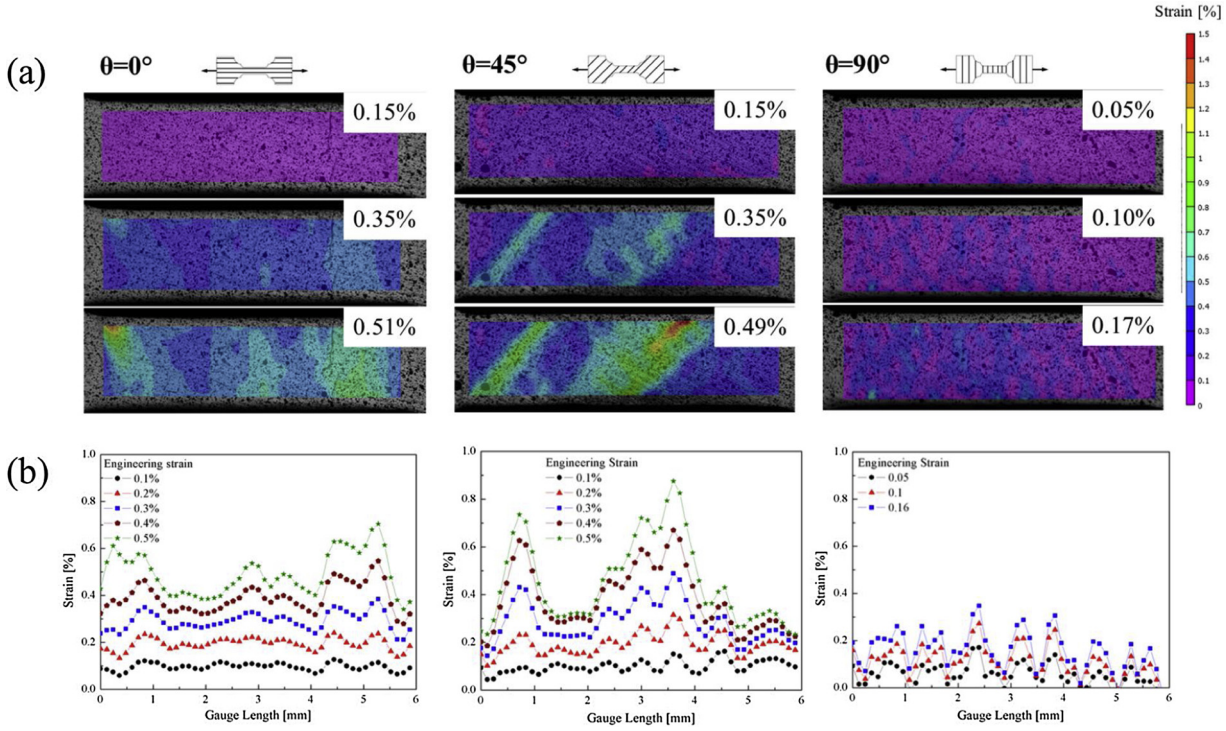

Fig. 8. (a) Strain distribution maps of as-deposited specimens with different loading directions (θ = 0°, θ = 45°, and θ = 90°) and (b) line scanning maps indicating strain variations in the gauge section of the associated specimens at different engineering strains.

$$G>0.617(100N_0)^{1/3}\left\{1-\frac{(\Delta T_N)^3}{(\Delta T_c)^3}\right\}\Delta T_c \quad (2)$$

where G is the thermal gradient, N_0 is the nuclei density, ΔT_N is the nucleation undercooling, and ΔT_c is the undercooling.

$$\Delta T_c = 2\left\{-\frac{2m(1-k_0)C_0V\Gamma}{D}\right\}^{1/2} \quad (3)$$

where m is the liquidus slope, k_0 is the distribution coefficient, C_0 is the alloy composition, V is the growth rate, Γ is the Gibbs–Thomson parameter, and D is the liquid diffusion coefficient. In this study, the parameter values for TiAl alloy are as follows: m = -8.53 K/at.%, k_0 = 0.88, $\Gamma = 10^{-7}$ m·K, $D = 5\times10^{-9}\,m^2{\cdot}s^{-1}$, $N_0 = 2\times10^{15}$, and ΔT_N = 2 K [33–35].

Based on the calculations using Hunt's model, we established a selection map of microstructural morphology for as-deposited TiAl alloys, as shown in Fig. 11a. Bontha's research [36] demonstrated that increasing laser power results in a substantial decrease in temperature gradient at all depths within the melt pool, whereas scanning speed influences both the temperature gradient and the growth rate. Thus, it is concluded that the temperature gradient and growth rate, which are the key parameters controlling microstructure in the DLD, are determined by processing parameters. The calculated solidification conditions varying with laser power and scanning speed were presented in ref. [36], and the blue scatter points in Fig. 11a were extracted to approximately evaluate the solidification conditions in our study. It can be seen that nearly the whole melt pool is located in the columnar grain zone, indicating that columnar grains are the dominant feature of the solidification microstructure, agreeing with the observed columnar colony morphology. Moreover, it is deduced that the α phase is the primary phase solidified from the liquid according to the characteristic of the orientated lamellar structure [37]. While cooling to room temperature, the α phase transforms into the α_2/γ lamellar structure, obeying the Blackburn orientation relationship: $\{111\}_\gamma \,||\, \{0001\}_{\alpha2}$ and $<1\bar{1}0>_\gamma \,||\, <11\bar{2}0>_{\alpha2}$, with the lamellar interface parallel to $\{0001\}_{\alpha2}$. As the α phase preferentially grows along the unique <0001> direction

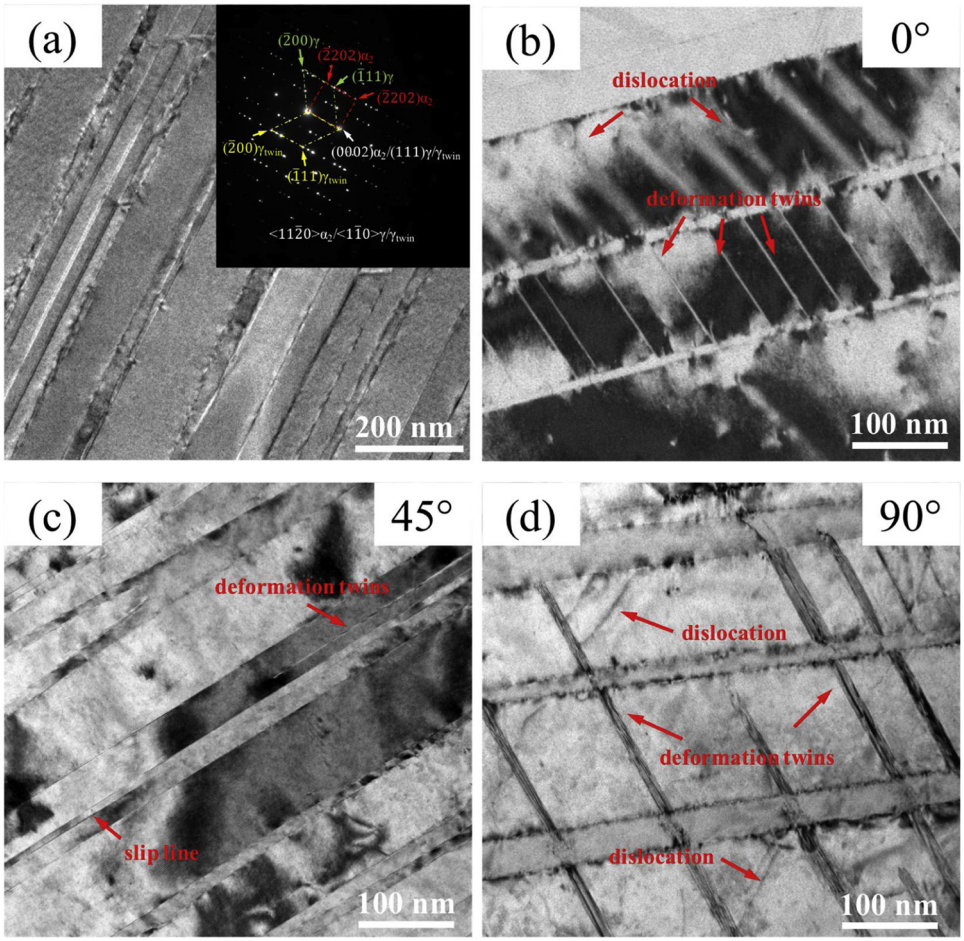

Fig. 9. TEM images of the coarse lamellar colony. (a) As-deposited specimen; (b)–(d) Deformed specimens with loading directions θ= 0°, 45°, and 90°, respectively.

from the bottom of the melt pool [38], all six transformed γ variants form perpendicularly to the columnar growth direction. Thus, they generate a directional aligned lamellar structure as reflected in Figs. 3d and 4 c. Furthermore, these γ variants can be classified into two twin groups. Each group is in accordance with one of the two disordered cubic variants in the (111) twin relationship on the basis of stacking sequence, which is usually present in a twinning relationship.

Second, the alternative-band microstructure composed of coarse lamellar colony bands and complicated microstructure bands is also a specific microstructural feature only observed in as-deposited Ti-47Al-2Cr-2Nb alloy. It is worth mentioning that the sum of the two adjacent alternative bands corresponds to single-layer thickness, implying a potential relationship between the particular microstructure and the one-by-one layer deposition process. A similar alternative-band microstructure was obtained by Todai et al. via electron-beam melting technology [39], although it comprised duplex-like bands and coarse γ grain bands. The authors attributed this feature to the effect of repeated local heat treatments during deposition, which can also explain the alternative-band microstructure observed in this study. A directional coarse columnar colony filled with a lamellar structure is formed in the melt pool when every new layer is deposited. Meanwhile, each laser scan brings a non-uniform heat treatment for the previously deposited layers. Previous research on post-weld heat treatments [40] demonstrated that heat treatment above 1000 °C contributes to the formation of equiaxed γ grains and the precipitation of banded lamellar grains, which is in accordance with the microstructure observed in the complicated microstructure band. Thus, it is deduced that the complicated microstructure band can be attributed to the non-uniform heat treatment that partly transforms the previously deposited layer, as shown in Fig. 11b. The regions significantly altered by heat treatment are called the heat-affected zones.

4.2. Deformation mechanism

As demonstrated in previous reports [40,41], the deformation is mainly confined to the majority γ(TiAl) phase, regardless of whether the alloy has a lamellar or equiaxed microstructure. Dislocation slips for the $L1_0$ type γ(TiAl) phase are usually inclined to occur on $\{111\}_\gamma$ planes along $<110>_\gamma$ directions, which are respectively the close-packed plane and close-packed direction. However, the particularity for γ-TiAl is that the $<110]_\gamma$ and $<101]_\gamma$ directions are crystallographically not equivalent because of the alternatingly arranged stacking sequence of Ti and Al atomic planes along the $<001>_\gamma$ direction. This results in two types of dislocations: ordinary dislocations whose Burgers vector is $\mathbf{b} = 1/2 < 110]_\gamma$ and superdislocations with Burgers vectors of $\mathbf{b} = 1/2 < 101]_\gamma$ and $\mathbf{b} = 1/2 < 11\bar{2}]_\gamma$. Moreover, there are four additional $\{111\} < 11\bar{2}>_\gamma$ twinning systems that can also operate. However, regarding the directional lamellar structure, as in our studies, the loading orientation plays a significant role in determining the critical stress of a deformation system at the early stages of deformation. This is because these available slip and twinning systems will interact differently with the lamellar interface. Lebensohn [42] developed a classification of these deformation systems, called morphology-based classification, as summarized in Table 2. The longitudinal system implies that both the slip plane and slip direction are parallel to the lamellar interface, and the mixed system indicates that the slip plane interacts with the lamellar interfaces. However, the slip direction is parallel to them. Systems in which the slip plane and slip direction interact with

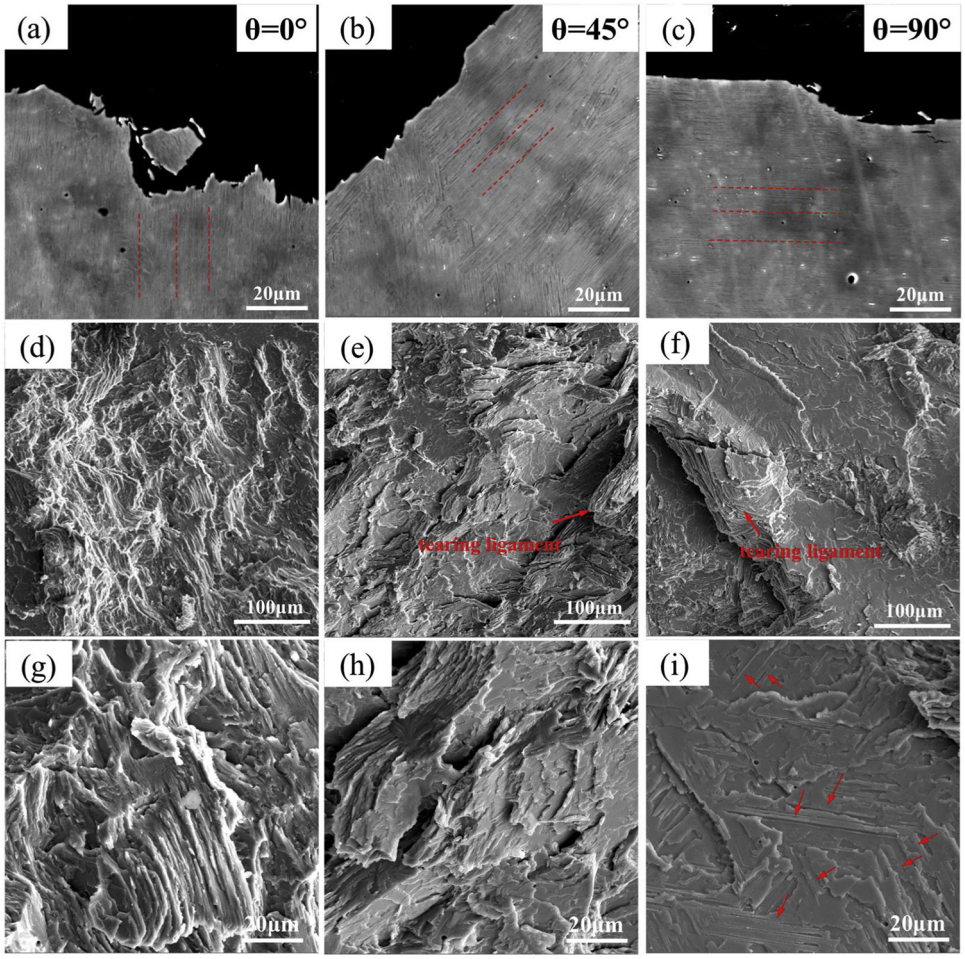

Fig. 10. SEM images of cross-section and fracture surface morphology of the specimens under different loading directions. (a), (d), (g) θ = 0°; (b), (e), (h) θ = 45°; (c), (f), (i) θ = 90°. The dotted lines in (a)–(c) represent the lamellar directions, and the red arrows in (i) show the nanolaths inserted in the γ plates. (For interpretation of the references to colour in this figure legend, the reader is referred to the web version of this article).

the lamellar interfaces are then grouped into the transverse system. Our study reveals that directional coarse lamellar colonies whose lamellar orientations are nearly parallel to the laser scanning direction constitute a majority of the as-deposited microstructure, meaning the corresponding deformation mechanism is analogous to that of polysynthetic twinned (PST) TiAl alloy. TEM observations indicate that, when the loading direction is θ= 45°, soft mode, longitudinal deformation systems are activated with slip plane and slip direction parallel to the lamellar interface, as shown in Fig. 9c. Scarcely any interactions between deformation systems and lamellar interfaces are observed. When the loading direction is θ= 0° or θ= 90°, which represents a hard mode, the longitudinal deformation systems are greatly

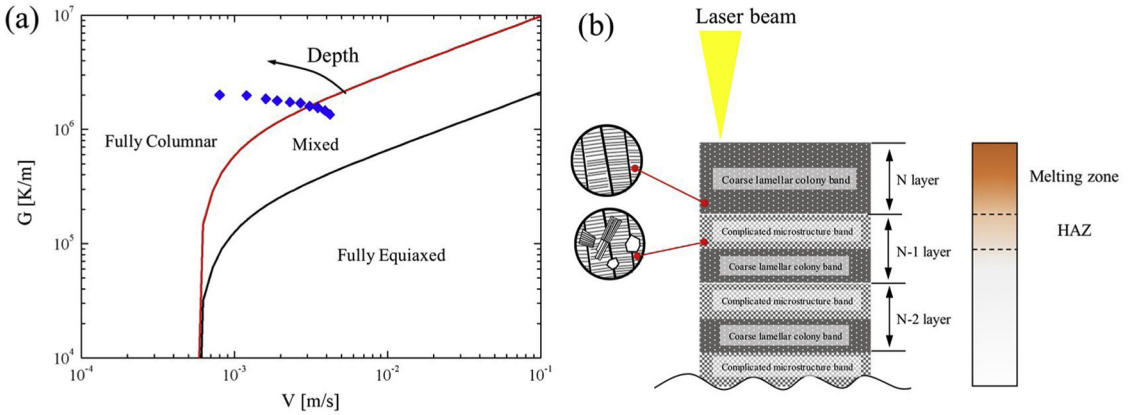

Fig. 11. (a) Selection map of microstructure morphology based on solidification conditions, including temperature gradient G and growth rate V. The blue scatter points in the selection map are calculation results for different melt-pool depths during laser deposition of thin-wall Ti alloys, which is in accordance with our process parameters and extracted from ref. [36]; (b) Schematic of the alternative-band microstructure formation mechanism during DLD. (For interpretation of the references to colour in this figure legend, the reader is referred to the web version of this article).

Table 2
Classification of deformation systems in fully lamellar structure of TiAl alloy and the associated Schmid factor with different tensile loading directions.

System	Morphology-based	Mechanism-based	Schmid Factor		
			θ = 0°	θ = 45°	θ = 90°
(111)[1$\bar{1}$0]	longitudinal system	ordinary slip	0	0.5	0
(111)[0$\bar{1}$1]	longitudinal system	super slip	0	0.5	0
(111)[$\bar{1}$01]	longitudinal system	super slip	0	0.5	0
($\bar{1}$11)[$\bar{1}$10]	mixed system	ordinary slip	0.471	0.360	0
($\bar{1}$11)[0$\bar{1}$1]	mixed system	super slip	0.471	0.360	0
(1$\bar{1}$1)[$\bar{1}$01]	mixed system	super slip	0.471	0.360	0
(1$\bar{1}$1)[110]	transverse system	ordinary slip	0.408	0.484	0.272
($\bar{1}$11)[110]	transverse system	ordinary slip	0.408	0.484	0.272
(1$\bar{1}$1)[011]	transverse system	super slip	0.408	0.484	0.272
($\bar{1}$11)[101]	transverse system	super slip	0.408	0.484	0.272
($\bar{1}$11)[011]	transverse system	super slip	0.408	0.484	0.272
($\bar{1}$11)[101]	transverse system	super slip	0.408	0.484	0.272
(111)[11$\bar{2}$]	longitudinal system	twinning	0	0.5	0
(1$\bar{1}$1)[11$\bar{2}$]	transverse system	twinning	0.494	0.258	0.272
($\bar{1}$11)[$\bar{1}$1$\bar{2}$]	transverse system	twinning	0.494	0.258	0.272
($\bar{1}$11)[1$\bar{1}$2]	transverse system	twinning	0.471	0.406	0.314

suppressed, and deformation twins that traverse the primary γ laths turn up. This phenomenon is strongly related to the Schmid factor, which provides an indication of how easy it is for a slip to occur for a particular system. The Schmid factor is calculated as $m = \cos\varphi\cos\lambda$, where φ is the angle between the loading direction and normal direction of the associated slip plane, and λ is the angle between the loading direction and slip direction. The calculated Schmid factors of each deformation system under different tensile orientations are listed in Table 2. The lamellae are assumed to be perfectly perpendicular to the building direction.

When the loading direction is θ= 45°, all the longitudinal deformation systems possess a maximum Schmid factor of 0.5, implying that the longitudinal deformation systems are easy to activate. Because the Schmid factors of transversal deformation systems are much lower, it is difficult to trigger the transverse deformation systems, as demonstrated in Fig. 9c. However, when the loading direction is turned to θ= 90°, it can be seen that the Schmid factors of longitudinal deformation systems and mixed deformation systems are equal to zero. This means these two kinds of deformation systems are greatly suppressed, and only transverse deformation systems can operate. When θ= 0°, mixed deformation systems and transverse deformation systems possess a high Schmid factor (0.47–0.49). However, longitudinal deformation systems have a Schmid factor of zero. That is why longitudinal deformation twins were rarely observed in this case.

The strengthening effect resulting from internal boundaries is usually described in terms of the Hall–Patch relationship, which is always expressed as $\sigma = \sigma_0 + kd^{-1/2}$, where σ_0 is a stress contribution independent of grain size, k is a material constant representing the difficulty of a slip penetrating from one grain to the next, and d is the grain size that essentially measures the free path of the slips in single grains. Thus, the strengthening effect can also be classified into three groups according to the different deformation mechanisms. When the loading is applied at θ= 45°, longitudinal deformation systems become the major deformation features, and the free paths of these slips are determined by the domain size (i.e., the long axis of the lamellae). However, when the loading is applied at θ= 90°, only transverse deformation systems are activated in the γ lamellae, implying that the free paths are confined by lamellar spacing. For the loading direction of θ= 0°, transverse deformation systems and mixed transverse systems are activated, and the effective slip paths are considered to be controlled by domain size and lamellar spacing. Therefore, it is deduced that loading along θ= 45° and θ= 90° will respectively contribute to a low and a high strength, and loading along θ= 0° will results in an intermediate strength because of the coefficient of domain size and lamellar spacing. These deductions have already been demonstrated in previous studies on PST TiAl alloys [42,43]. However, it seems to contradict our tensile results. This phenomenon should be attributed to the specific alternative-band microstructure and fracture behaviors, which are discussed in the next section.

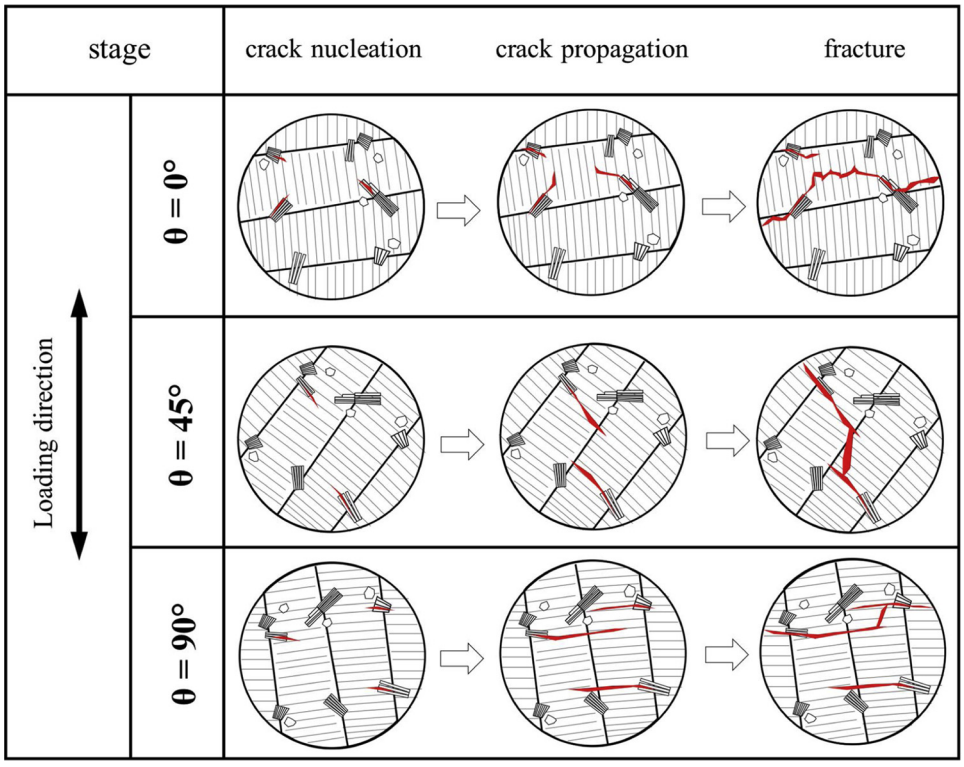

Fig. 12. Schematic of the fracture mechanism for the as-deposited alternative-band microstructure of Ti-47Al-2Cr-2Nb alloy under different loading directions.

4.3. Fracture behavior

The above observation reveals that the as-deposited Ti-47Al-2Cr-2Nb alloy exhibits a specific alternative-band microstructure, comprising complicated microstructure bands and coarse lamellar colony bands. Hardness measurements show that the micro-hardness periodically varied along the building direction, with the complicated microstructure bands possessing a relatively low hardness and the coarse lamellar colony bands exhibiting a high hardness. As hardness is proportional to yield strength [44], it is concluded that the complicated microstructure bands can bear relatively low stress compared with the coarse lamellar colony bands. This implies that cracks are always initiated in the complicated microstructure band, as shown in Fig. 12. Then, the following crack propagation mode determines the ultimate strength and elongation. It is a consensus that there are six γ variants generated from an α/α_2 matrix, according to the Blackburn orientation relationship. In addition to the α_2/γ boundary, three types of γ/γ interfaces form a true twin interface, a pseudo-twin interface, and a 120° ordered interface. Their cleavage energies can be expressed as follows:

$$G_i = G_c - \Gamma_i - E_m \quad (4)$$

where G_c is the ideal cleavage energy of the {111} plane, Γ_i is the interfacial energy that varies with the interface type, and E_m is the misfit energy estimated using the Frack and Van de Merwe method [45]. Thus, the cleavage energy of these lamellar interfaces is lower than that of the common cleavage plane {111}, suggesting a cracking priority along these interfaces. When θ= 45° or θ= 90°, the cracks will propagate along the lamellar interface under the effect of normal stress. Because these cracks are usually noncoplanar, they will finally link to each other through the tearing ligament, as shown in Fig. 12. The associated fracture toughness is low under these two circumstances. Once cracks initiate, they propagate rapidly and contribute to fracturing. This is why their ultimate strength is relatively low. However, when the loading direction is parallel to the lamellar orientation (θ= 0°), the normal stress applied to the lamellar interface is very low, and it is difficult for cracks to propagate along the lamellar interfaces. As the external stress increases to a higher level, other cleavage planes in the α_2 and γ laths are activated, leading the cracks to traverse these lamellar structures. Because the propagation of translamellar cracks is strongly blocked by α_2/γ or γ/γ interfaces, the fracture resistance is considerably increased. During this process, more slip and twinning deformation systems are generated, which explains the high ultimate strength and strain when the loading direction is θ= 0°.

5. Conclusions

Single-track Ti-47Al-2Cr-2Nb alloy walls were additively manufactured using DLD technology. The microstructure characterization of OM, SEM, and EBSD were performed, and the anisotropic tensile behavior was investigated by applying different loading directions. The main findings can be concluded as follows:

1 The as-deposited Ti-47Al-2Cr-2Nb alloy specimens exhibited a particular alternative-band microstructure comprising complicated microstructure bands and coarse lamellar colony bands. Fine equiaxed γ grains, feathery microstructures, Widmanstatten laths, and coarse lamellar colonies constituted the complicated microstructure band. The coarse lamellar colony band completely consisted of coarse lamellar colonies in which all laths were nearly perpendicular to the building direction. This unique alternative-band microstructure resulted from the combined effects of rapid solidification and cyclic heat treatment derived from exposure to multiple laser scans.
2 The ultimate strength and elongation of the as-deposited Ti-47Al-2Cr-2Nb alloy specimens varied significantly with the angle (θ) between the loading direction and the substrate. When the loading direction was parallel to the substrate (θ= 0°), the specimen had the maximum ultimate strength and elongation (706 MPa and 0.51 %), and TEM observations revealed that dislocations and transverse twinning systems were activated. The ultimate strength and elongation dropped sharply to the minimum (273 MPa and 0.16 %) when the loading direction was turned perpendicular to the substrate (θ= 90°), in which the strain predominantly came from the transverse deformation systems. In the middle state with the loading orientation of 45°, the ultimate strength was about 358 MPa, and the relative higher elongation of 0.49 % was mainly associated with the strain coming from the longitudinal deformation systems.
3 The fracture surface observations and cleavage energy analysis indicate that the cracks preferentially propagated along the lamellar interface and finally linked to each other by tearing ligaments when the loading direction was 45° and 90°. However, cracks were blocked by the lamellar interface and usually propagated by traversing the α_2/γ laths when the loading direction was 0°. The crack propagation mechanism proposed here can reasonably explain the anisotropic behavior of specimens with alternative-band microstructure, fabricated by DLD.

CRediT authorship contribution statement

Xinyu Zhang: Investigation, Data curation, Writing - original draft. **Chuanwei Li:** Conceptualization, Methodology, Supervision. **Mengyao Zheng:** Investigation, Data curation. **Zhenhua Ye:** Formal analysis, Software. **Xudong Yang:** Investigation, Validation. **Jianfeng Gu:** Supervision, Writing - review & editing.

Declaration of Competing Interest

There are no conflicts of interest.

Acknowledgments

The authors acknowledge financial support from the National Natural Science Foundation of China (Grant No. 51971145).

References

[1] H. Clemens, S. Mayer, Design, processing, microstructure, properties, and applications of advanced intermetallic TiAl alloys, Adv. Eng. Mater. 15 (4) (2013) 191–215.
[2] K. Kothari, R. Radhakrishnan, N.M. Wereley, Prog. Aerosp. Sci. 55 (2012) 1–16.
[3] D. Herzog, V. Seyda, E. Wycisk, C. Emmelmann, Acta Mater. 117 (15) (2016) 371–392.
[4] S.M. Thompson, L. Bian, N. Shamsaei, A. Yadollahi, An overview of direct laser deposition for additive manufacturing part I: transport phenomena, modeling and diagnostics, Addit. Manuf. 8 (2015) 36–62.
[5] Y. Zhu, J. Li, X. Tian, H. Wang, D. Liu, Microstructure and mechanical properties of hybrid fabricated Ti–6.5Al–3.5Mo–1.5Zr–0.3Si titanium alloy by laser additive manufacturing, Mater. Sci. Eng. A 607 (23) (2014) 427–434.
[6] M.J. Bermingham, D.H. StJohn, J. Krynen, S. Tedman–Jones, M.S. Dargusch, Controlling the microstructure and properties of wire arc additive manufactured Ti–6Al–4V with trace boron additions, Acta Mater. 168 (1) (2019) 261–271.
[7] M.L. Griffith, M.T. Ensz, J.D. Puskar, C.V. Robino, J.A. Brooks, J.A. Philliber, J.E. Smugeresky, W.H. Hofmeister, Understanding the microstructure and properties of components fabricated by laser engineered net shaping (LENS), Mater. Res. Soc. 625 (2000) 9–20.
[8] J. Yu, M. Rombouts, G. Maes, Cracking behavior and mechanical properties of austenitic stainless steel parts produced by laser metal deposition, Mater. Des. 45 (2013) 228–235.
[9] Z. Wang, T.A. Palmer, A.M. Beese, Effect of processing parameters on microstructure and tensile properties of austenitic stainless steel 304L made by directed energy deposition additive manufacturing, Acta Mater. 110 (15) (2016) 226–235.
[10] Zhu Y, X. Tian, J. Li, H. Wang, The anisotropy of laser melting deposition additive manufacturing Ti–6.5Al–3.5Mo–1.5Zr–0.3Si titanium alloy, Mater. Des. 67 (2015) 538–542.
[11] B.E. Carroll, T.A. Palmer, A.M. Beese, Anisotropic tensile behavior of Ti–6Al–4V components fabricated with directed energy deposition additive manufacturing, Acta Mater. 87 (1) (2015) 309–320.
[12] J. Schwerdtfeger, C. Körner, Selective electron beam melting of Ti–48Al–2Nb–2Cr: microstructure and aluminium loss, Intermetallics 49 (2014) 29–35.

[13] W. Li, J. Liu, Y. Zhou, S. Wen, Q. Wei, C. Yan, Y. Shi, Effect of substrate preheating on the texture, phase and nanohardness of a Ti–45Al–2Cr–5Nb alloy processed by selective laser melting, Scr. Materialia 118 (2016) 13–18.
[14] W. Li, J. Liu, S. Wen, Q. Wei, C. Yan, Y. Shi, Crystal orientation, crystallographic texture and phase evolution in the Ti–45Al–2Cr–5Nb alloy processed by selective laser melting, Mater. Charact. 113 (2016) 125–133.
[15] W. Li, J. Liu, Y. Zhou, S. Wen, J. Tan, S. Li, Q. Wei, C. Yan, Y. Shi, Texture evolution, phase transformation mechanism and nanohardness of selective laser melted Ti-45Al-2Cr-5Nb alloy during multi-step heat treatment process, Intermetallics 85 (2017) 130–138.
[16] W. Li, Y. Yang, J. Liu, Y. Zhou, M. Li, S. Wen, Q. Wei, C. Yan, Y. Shi, Enhanced nanohardness and new insights into texture evolution and phase transformation of TiAl/TiB2 in-situ metal matrix composites prepared via selective laser melting, Acta Mater. 136 (1) (2017) 90–104.
[17] M. Thomas, T. Malot, P. Aubry, Laser metal deposition of the intermetallic TiAl alloy, Metall. Mater. Trans. A 48 (6) (2017) 3143–3158.
[18] H.P. Tang, G.Y. Yang, W.P. Jia, W.W. He, S.L. Lu, M. Qian, Additive manufacturing of a high niobium-containing titanium aluminide alloy by selective electron beam melting, Mater. Sci. Eng. A 636 (2015) 103–107.
[19] J. Gussone, Y.C. Hagedorn, H. Gherekhloo, G. Kasperovich, T. Merzouk, J. Hausmann, Microstructure of γ-titanium aluminide processed by selective laser melting at elevated temperatures, Intermetallics 66 (2015) 133–140.
[20] G. Yang, H. Kou, J. Yang, J. Li, H. Fu, Microstructure control of Ti45Al8.5Nb(W, B, Y) alloy during the solidification process, Acta Mater. 112 (15) (2016) 121–131.
[21] J.C. Schuster, M. Palm, Reassessment of the binary Aluminum-Titanium phase diagram, J. Phase Equilib. Diffus. 27 (3) (2006) 255–277.
[22] S.R. Dey, A. Hazotte, E. Bouzy, Crystallography and phase transformation mechanisms in TiAl-based alloys – a synthesis, Intermetallics 17 (12) (2009) 1052–1064.
[23] W. Zhao, Y. Pei, D. Zhang, Y. Ma, S. Gong, H. Xu, The microstructure and tensile property degradation of a gamma-TiAl alloy during isothermal and cyclic high temperature exposures, Intermetallics 19 (3) (2011) 429–432.
[24] J.C. Han, S.L. Xiao, J. Tian, Y.Y. Chen, L.J. Xu, X.P. Wang, Y. Jia, S.Z. Cao, Microstructure characterization and tensile properties of a Ni-containing TiAl-based alloy with heat treatment, Rare Metals 35 (1) (2016) 26–34.
[25] M. Su, Z. Lang, L. Zheng, J. Yan, K. Guan, H. Zhang, Effect of heat treatment on microstructures and mechanical properties in a full lamellar PM TiAl alloy, Mater. Res. 15 (3) (2012) 455–460.
[26] Q. Wang, H. Ding, H. Zhang, R. Chen, J. Guo, H. Fu, Variations of microstructure and tensile property of γ-TiAl alloys with 0 ~ 0.5 at% C additives, Mater. Sci. Eng. A 700 (2017) 198–208.
[27] Y. Liu, R. Hu, J. Yang, J. Li, Tensile properties and fracture behavior of in-situ synthesized Ti2AlN/Ti48Al2Cr2Nb composites at room and elevated temperatures, Mater. Sci. Eng. A 679 (2016) 7–13.
[28] B. Lin, R. Liu, Q. Jia, Y. Cui, P.A. Withey, R. Yang, Effect of yttria inclusion on room temperature tensile properties of investment cast TiAl, Mater. Sci. Eng. A 712 (2018) 73–79.
[29] A. Couret, G. Molenat, J. Galy, M. Thomas, Microstructures and mechanical properties of TiAl alloys consolidated by spark plasma sintering, Intermetallics 16 (9) (2008) 1134–1141.
[30] J.D. Hunt, Steady state columnar and equiaxed growth of dendrites and eutectic, Mater. Sci. Eng. 65 (1) (1984) 75–83.
[31] M. Gaumann, C. Bezencon, P. Canalis, W. Kurz, Single-crystal laser deposition of superalloys: processing–microstructure maps, Acta Mater. 49 (6) (2001) 1051–1062.
[32] Z. Liu, H. Qi, Effects of substrate crystallographic orientations on crystal growth and microstructure formation in laser powder deposition of nickel-based superalloy, Acta Mater. 87 (1) (2015) 248–258.
[33] Y. Su, C. Liu, X. Li, J. Guo, B. Li, J. Jia, H. Fu, Microstructure selection during the directionally peritectic solidification of Ti–Al binary system, Intermetallics 13 (3-4) (2005) 267–274.
[34] D.R. Liu, J.J. Guo, S.P. Wu, Y.Q. Su, H.Z. Fu, Stochastic modeling of columnar-to-equiaxed transition in Ti–(45–48 at%) Al alloy ingots, Mater. Sci. Eng. A 415 (1-2) (2006) 184–194.
[35] D.R. Johnson, H. Inui, M. Yamaguchi, Crystal growth of TiAl alloys, Intermetallics 6 (7-8) (1998) 647–652.
[36] S. Bontha, N.W. Klingbeil, P.A. Kobryn, H.L. Fraser, Thermal process maps for predicting solidification microstructure in laser fabrication of thin-wall structures, J. Mater. Process. Tech. 178 (1-3) (2006) 135–142.
[37] M. Yamaguchi, D.R. Johnson, H.N. Lee, H. Inui, Directional solidification of TiAl-base alloys, Intermetallics 8 (5-6) (2000) 511–517.
[38] M.C. Flemings, Solidification Processing, McGraw–Hill, 1974.
[39] M. Todai, T. Nakano, T. Liu, H.Y. Yasuda, K. Hagihara, K. Cho, M. Ueda, M. Takeyama, Effect of building direction on the microstructure and tensile properties of Ti-48Al-2Cr-2Nb alloy additively manufactured by electron beam melting, Add. Manufact. 13 (2016) 61–70.
[40] H. Inui, A. Nakamura, M.H. Oh, M. Yamaguchi, Deformation structures in ti-rich tial polysynthetically twinned crystals, Philos. Mag. A 66 (4) (1992) 557–573.
[41] F. Appel, U. Brossmann, U. Christoph, S. Eggert, P. Janschek, U. Lorenz, J. Mullanuer, M. Oehring, J.D. Paul, Recent progress in the development of gamma titanium aluminide alloys, Adv. Eng. Mater. 2 (11) (2000) 699–720.
[42] R. Lebensohn, H. Uhlenhut, C. Hartig, H. Mecking, Plastic flow of γ -TiAl-based polysynthetically twinned crystals: micromechanical modeling and experimental validation, Acta Mater. 46 (13) (1999) 4701–4709.
[43] J.P. Alberto, T.P. Maria, J.M. Molina–Aldareguia, Effect of lamellar orientation on the strength and operating deformation mechanisms of fully lamellar TiAl alloys determined by micropillar compression, Acta Mater. 123 (15) (2017) 102–114.
[44] R. Chen, D. Zheng, J. Guo, T. Ma, H. Ding, Y. Su, H. Fu, A novel method for grain refinement and microstructure modification in TiAl alloy by ultrasonic vibration, Mater. Sci. Eng. A 653 (20) (2016) 23–26.
[45] Y.H. Lu, Y.G. Zhang, L.J. Qiao, Y.B. Wang, C.Q. Chen, W.Y. Chu, In situ TEM study of fracture mechanisms of polysynthetically twinned (PST) crystals of TiAl alloys, Mater. Sci. Eng. A 289 (1-2) (2000) 91–98.